

Solving hadron structures with variational quantum eigensolvers

Wenyang Qian,^{1,2,*} Robert Basili,^{1,2,†} Soham Pal,^{2,‡} Glenn Luecke,^{1,§} and James P. Vary^{2,¶}

¹*Department of Mathematics, Iowa State University, Ames, IA 50011, USA*

²*Department of Physics and Astronomy,
Iowa State University, Ames, IA 50011, USA*

(Dated: December 6, 2021)

Quantum computing has demonstrated the potential to revolutionize our understanding of nuclear, atomic, and molecular structure by obtaining forefront solutions in non-relativistic quantum many-body theory. In this work, we show that quantum computing can be used to solve for the structure of hadrons, governed by strongly-interacting relativistic quantum field theory. Following our previous work on light unflavored mesons as a relativistic bound-state problem within the nonperturbative Hamiltonian formalism, we present the numerical calculations on simulated quantum devices using the basis light-front quantization (BLFQ) approach. We implement and compare the variational quantum eigensolver (VQE) and the subspace-search variational quantum eigensolver (SSVQE) to find the low-lying mass spectrum of the light meson system and its corresponding light-front wave functions (LFWFs) via quantum simulations. Based on these LFWFs, we then evaluate the meson decay constants and parton distribution functions. Our quantum simulations are in reasonable agreement with accurate numerical solutions on classical computers, and our overall results are comparable with the available experimental data.

I. INTRODUCTION

Quantum computing has emerged as a new method to simulate large-scale many-body quantum systems, which is a core challenge in the fields of chemistry and physics. Possessing the very same quantum mechanical nature that modern computational models of quantum systems seek to emulate (usually at great cost), quantum computing is considered a natural candidate for overcoming current resource-barriers faced by those models. In the current Noisy Intermediate-Scale Quantum (NISQ) era [1], our goal is to make full use of the available quantum computing resources to develop techniques for applications compatible with the noise of early quantum hardware. In addition to their necessity for achieving early quantum advantage, developing these techniques provide critical experience, insight, and points of comparison for later approaches to be applied with fault-tolerant quantum computation when it becomes available in the future.

* wqian@iastate.edu

† basiliro@iastate.edu

‡ soham@iastate.edu

§ grl@iastate.edu

¶ jvary@iastate.edu

Most current quantum computing applications for many-body systems rely on hybrid quantum-classical computers, such as the quantum approximate optimization algorithm (QAOA) [2] and the variational quantum eigensolver (VQE) [3–5]. The VQE algorithm was initially proposed to solve quantum chemistry problems [3, 6] and has now been applied to find the ground state energy of various nuclear systems [7–9]. In addition to obtaining ground states, the VQE algorithm can also be extended to solve for excited states [10–16]. In particular, the recently-proposed subspace-search variational quantum eigensolver (SSVQE) takes advantage of the orthogonality of the reference states and produces the specified spectroscopy in a single optimization step [15].

Light-front Hamiltonian approaches are particularly well-suited to quantum computing applications [8, 9, 17] as the eigenvalues of the Hamiltonian give rise to the complete spectroscopy and the light-front wave functions (LFWFs) enable direct access to physical observables. One such light-front Hamiltonian formalism is the basis light-front quantization (BLFQ) approach. The BLFQ approach utilizes basis functions to exploit the symmetry of the system to achieve a numerical advantage in high-performance computing [18], and it has already been successfully applied to many relativistic and strongly-interacting bound state systems [19–28]. In addition to obtaining the hadron mass spectroscopy, observables such as the decay constants, electromagnetic form factors, parton distribution functions, and parton distribution amplitudes can also be computed conveniently with LFWFs. In our previous work with BLFQ [28], we applied an effective light-front Hamiltonian to the light unflavored meson system to obtain the mass spectroscopy and physical observables for the low-lying states. By modifying the same effective Hamiltonian to a practical basis size allowed by quantum simulators of currently available quantum computers, we investigate the mass spectroscopy and decay constants for the hadron system using the VQE and SSVQE approaches.

In this work, we will formulate the relativistic bound state problem of light meson systems and implement suitable VQE and SSVQE programs to obtain the mass spectroscopy as well as other physical observables such as the decay constants. Our aim is to demonstrate a feasible path for solving the properties of hadrons on quantum computers which could lead to quantum advantage on future systems. At the same time, we will benchmark two of the available options, VQE and SSVQE, with simulations for currently available systems.

We organize this paper as follows: In Sect. II, we introduce the effective Hamiltonian and BLFQ approach used to solve the light-front mass eigenvalue equation in the valence Fock sector of light-unflavored mesons. In Sect. III, we describe our implementation of the VQE and SSVQE methods to solve the bound-state eigenvalue problem, along with discussions of various encoding schemes and unitary ansatzes. In Sect. IV, we present the results of the mass spectroscopy and the decay constants for the selected states using VQE and SSVQE approaches on the light meson systems via quantum simulations and compare them to experiments and with the exact results obtained using classical methods. In Sect. V, we summarize our results and discuss possible future developments.

II. EFFECTIVE HAMILTONIAN AND BASIS FUNCTION REPRESENTATION

II.1. The Hamiltonian

We adopt the formalism and effective Hamiltonian for light unflavored meson systems proposed in a previous work [28]. The effective light-front Hamiltonian in a convenient but mixed representation (both momenta and coordinates are employed) reads

$$\begin{aligned}
H_{\text{eff}} &\equiv P^+ P_{\text{eff}}^- - \mathbf{P}_{\perp}^2 \\
&= \frac{\mathbf{k}_{\perp}^2 + m_q^2}{x} + \frac{\mathbf{k}_{\perp}^2 + m_{\bar{q}}^2}{1-x} + \kappa^4 x(1-x) \mathbf{r}_{\perp}^2 \\
&\quad - \frac{\kappa^4}{(m_q + m_{\bar{q}})^2} \partial_x (x(1-x) \partial_x) \\
&\quad - \frac{C_F 4\pi\alpha_s(Q^2)}{Q^2} \bar{u}_{s'}(k') \gamma_{\mu} u_s(k) \bar{v}_{\bar{s}}(-k) \gamma^{\mu} v_{\bar{s}'}(-k'), \tag{1}
\end{aligned}$$

where m_q ($m_{\bar{q}}$) is the mass of the quark (anti-quark), κ is the strength of the confinement, \mathbf{k}_{\perp} ($-\mathbf{k}_{\perp}$) is the relative momentum of the quark (anti-quark), x ($1-x$) is the longitudinal momentum fraction of the quark (anti-quark), and \mathbf{r}_{\perp} is the transverse separation of the quark and the anti-quark. The first two terms are the light-front kinetic energy of the quark and the anti-quark. The third term adopts the light-front anti-de Sitter/quantum chromodynamics (AdS/QCD) soft-wall potential [29, 30] to implement the transverse confinement. The fourth term serves as the longitudinal confinement [20] by supplementing the transverse confinement to form a 3-dimensional spherical confinement potential in the non-relativistic limit. The fifth and last term is the one-gluon exchange based on one-loop perturbative QCD (pQCD) [21] to produce spin-dependent interactions at short distance, where $C_F = (N_c^2 - 1)/(2N_c) = 4/3$ is the color factor with $N_c = 3$, and Q^2 is the average 4-momentum square carried by the exchanged gluon. It is important to note that the contribution of the pseudoscalar interaction in the original paper is neglected, since we will be using very limited basis spaces to perform quantum simulation in this work.

With the Hamiltonian defined in Eq. (1), the mass spectrum and wave functions can be obtained directly by solving the light-front eigenvalue equation

$$H_{\text{eff}} |\psi(P, j, m_j)\rangle = M^2 |\psi(P, j, m_j)\rangle, \tag{2}$$

where $P = (P^-, P^+, \mathbf{P}_{\perp})$ is the four momentum of the hadron in light-front coordinates (Appendix A), j is the total angular momentum, m_j is the magnetic projection, and M is the mass of the hadron. Working within the leading $|q\bar{q}\rangle$ Fock sector, the

meson state is written as

$$\begin{aligned}
|\psi(P, j, m_j)\rangle &= \sum_{s, \bar{s}} \int \frac{dx}{2x(1-x)} \int \frac{d^2\mathbf{k}_\perp}{(2\pi)^3} \psi_{s\bar{s}}^{m_j}(\mathbf{k}_\perp, x) \\
&\times \frac{1}{\sqrt{N_c}} \sum_{i=1}^{N_c} b_{si}^\dagger(xP^+, \mathbf{k}_\perp + x\mathbf{P}_\perp) \\
&\times d_{\bar{s}i}^\dagger((1-x)P^+, -\mathbf{k}_\perp + (1-x)\mathbf{P}_\perp) |0\rangle, \tag{3}
\end{aligned}$$

where $\psi_{s\bar{s}}^{m_j}(\mathbf{k}_\perp, x)$ is the light-front wave function (LFWF) of the hadron, s and \bar{s} represent the spin of the quark and anti-quark, and the quark and anti-quark creation operators b^\dagger and d^\dagger satisfy the canonical anti-commutation relations,

$$\begin{aligned}
\{b_{si}(p^+, \mathbf{p}_\perp), b_{s'i'}^\dagger(p'^+, \mathbf{p}'_\perp)\} &= \{d_{si}(p^+, \mathbf{p}_\perp), d_{s'i'}^\dagger(p'^+, \mathbf{p}'_\perp)\} \\
&= 2p^+(2\pi)^3 \delta(p^+ - p'^+) \delta^2(\mathbf{p}_\perp - \mathbf{p}'_\perp) \delta_{ss'} \delta_{ii'}. \tag{4}
\end{aligned}$$

II.2. Basis Function Representation

To solve the eigenvalue equation in Eq. (2), we use basis light-front quantization (BLFQ) approach, where the Hamiltonian is diagonalized within a chosen basis function representation [18]. In this work, we use the same basis function adopted in Ref. [28] which are convenient basis functions for the relative motion dynamics. That is, the center-of-mass motion does not appear since H_{eff} acts only on the relative motion of the quark and anti-quark. Explicitly, we expand the LFWF $\psi_{s\bar{s}}^{m_j}(\mathbf{k}_\perp, x)$ into the transverse and longitudinal basis functions with coefficients $\tilde{\psi}_{s\bar{s}}^{m_j}(n, m, l)$:

$$\psi_{s\bar{s}}^{m_j}(\mathbf{k}_\perp, x) = \sum_{nml} \tilde{\psi}_{s\bar{s}}^{m_j}(n, m, l) \phi_{nm}\left(\frac{\mathbf{k}_\perp}{\sqrt{x(1-x)}}\right) \chi_l(x), \tag{5}$$

where

$$\phi_{nm}(\mathbf{q}_\perp) = \frac{1}{\kappa} \sqrt{\frac{4\pi n!}{(n+|m|)!}} \left(\frac{q_\perp}{\kappa}\right)^{|m|} e^{-\frac{q_\perp^2}{2\kappa^2}} L_n^{|m|}\left(\frac{q_\perp^2}{\kappa^2}\right) e^{im\theta_q}, \tag{6}$$

$$\begin{aligned}
\chi_l(x; \alpha, \beta) &= x^{\frac{\beta}{2}} (1-x)^{\frac{\alpha}{2}} P_l^{(\alpha, \beta)}(2x-1) \sqrt{4\pi(2l+\alpha+\beta+1)} \\
&\times \sqrt{\frac{\Gamma(l+1)\Gamma(l+\alpha+\beta+1)}{\Gamma(l+\alpha+1)\Gamma(l+\beta+1)}}. \tag{7}
\end{aligned}$$

In the transverse direction, we use the 2-dimensional harmonic oscillator function $\phi_{nm}(\mathbf{q}_\perp)$, where $\mathbf{q}_\perp \triangleq \mathbf{k}_\perp/\sqrt{x(1-x)}$, $q_\perp = |\mathbf{q}_\perp|$, $\theta_q = \arg \mathbf{q}_\perp$, and $L_n^a(z)$ is the generalized Laguerre polynomial. The confining strength κ serves as the harmonic oscillator scale parameter. Integers n and m represent the principal quantum number for radial excitations and the orbital angular momentum projection quantum number, respectively. In the longitudinal direction, we use the basis function $\chi_l(x; \alpha, \beta)$, where l is the longitudinal quantum number, $P_l^{(\alpha, \beta)}(2x-1)$ is the Jacobi polynomial, $\alpha =$

$2m_{\bar{q}}(m_q + m_{\bar{q}})/\kappa^2$ and $\beta = 2m_q(m_q + m_{\bar{q}})/\kappa^2$. In particular, the basis function is constructed to preserve the magnetic projection of total angular momentum, $m_j = m + s + \bar{s}$.

The basis function approach offers a numerically efficient way to discretize the Hamiltonian. In practice, the transverse and longitudinal basis functions are truncated to their respective transverse cutoff N_{\max} and longitudinal cutoff L_{\max} :

$$2n + |m| + 1 \leq N_{\max}, \quad 0 \leq l \leq L_{\max}. \quad (8)$$

N_{\max} controls the total allowed oscillator quanta in the system and L_{\max} controls the longitudinal basis resolution. The exact spectra and LFWFs correspond to results without cutoffs, i.e. the infinite matrix limit or the continuum limit. It is anticipated that quantum computers will someday surpass classical computers and more closely approach the continuum limit.

III. VARIATIONAL QUANTUM EIGENSOLVER

Having defined the eigen-problem and its basis representation, we are ready to describe the variational quantum eigensolver approaches that we adopt to perform quantum simulations.

III.1. Variational Quantum Eigensolver

Given a Hermitian matrix H with an unknown minimum eigenvalue λ_{\min} associated with the eigenstate $|\psi_{\min}\rangle$, the variational principle provides an estimate λ_{θ} upperbounding λ_{\min} ,

$$\lambda_{\min} \leq \lambda_{\vec{\theta}} \equiv \langle \psi(\vec{\theta}) | \hat{H} | \psi(\vec{\theta}) \rangle, \quad (9)$$

where $\vec{\theta}$ is a list of parameters, and $|\psi(\vec{\theta})\rangle$ is a parameterized eigenstate associated with $\lambda_{\vec{\theta}}$.

The variational quantum eigensolver (VQE) [3, 31] is a hybrid computational approach consisting of a quantum part and a classical part. In the quantum part, a prepared parameterized quantum circuit, represented by the unitary $\hat{U}(\vec{\theta})$, is applied to an initial state, $|\psi_0\rangle$, to obtain a final state, $|\psi(\vec{\theta})\rangle \equiv \hat{U}(\vec{\theta})|\psi_0\rangle$, that estimates $|\psi_{\min}\rangle$. In the classical part, the estimate is iteratively optimized using a classical optimizer by changing the parameter $\vec{\theta}$ in each iteration to minimize the expectation value of the Hamiltonian, $\langle \psi(\vec{\theta}) | \hat{H} | \psi(\vec{\theta}) \rangle$. The algorithm terminates when a specified numerical tolerance or a maximum allowed iteration is achieved.

Specifically, the general procedure for solving an eigenvalue Hamiltonian problem with the VQE approach can be divided as follows:

1. Select the Hamiltonian \hat{H} for the targeted physical system and a suitable mapping scheme onto a set of qubits.
2. Pick an initial state $|\psi_0\rangle$ and a parameterized unitary ansatz $\hat{U}(\vec{\theta})$ for state evolution.

3. Apply the unitary ansatz to the initial state to obtain the final state $|\psi(\vec{\theta})\rangle = \hat{U}(\vec{\theta})|\psi_0\rangle$ and measure the cost function, or the expectation value of the Hamiltonian $\langle\psi(\vec{\theta})|\hat{H}|\psi(\vec{\theta})\rangle$. (quantum computer)
4. Optimize the parameter $\vec{\theta}$ by minimizing the cost function which is the expectation value. (classical computer)

Step 1 and 2 can usually be prepared before the actual VQE iterations. Each measurement in step 3 is ideally performed on the quantum computer by running repeated instances (or ‘shots’) of the quantum circuit to sample the probability distribution of the final state, and step 4 is computed on the classical computer using various optimizers available. In the end, both step 3 and 4 are repeated over many iterations to obtain the final optimal parameter θ^* . Optimization can be made in each step to improve the overall performance.

III.2. Subspace-search Variational Quantum Eigensolver

The VQE approach can be further extended to the subspace-search variational quantum eigensolver (SSVQE) [15] to find excited states of the system by restricting the subspace of unitary evolution and by considering a different set of cost functions. One variant of this approach is the weighted SSVQE. Instead of minimizing a single expectation value of the Hamiltonian, weighted SSVQE considers the cost function to be a weighted sum of a set of expectation values of the Hamiltonian, each measured from an orthogonal initial reference state after the unitary evolution. To find up to the k th excited states, the algorithm is as follows:

1. Select the Hamiltonian \hat{H} for the targeted physical system and a suitable mapping scheme onto a set of qubits.
2. Pick a set of mutually orthogonal initial states $\{|\psi_i\rangle\}_{i=0}^k$, and a parameterized unitary ansatz $\hat{U}(\vec{\theta})$ acting on these states.
3. Apply the unitary ansatz to each state and measure their expectation values, $\vec{E} = (E_0, E_1, \dots, E_k)$, where $E_i = \langle\psi_i(\vec{\theta})|\hat{H}|\psi_i(\vec{\theta})\rangle$. (quantum computer)
4. Optimize the parameter $\vec{\theta}$ by minimizing the cost function $\mathcal{C}_{\vec{\omega}}(\vec{\theta}) = \vec{\omega} \cdot \vec{E}$, where $\vec{\omega}$ is a straightly decreasing weight vector prioritizing lower-lying states ($\omega_i > \omega_j$ for $i < j$). (classical computer)

In particular, if we only look for the k th excited state, we need to modify the weight vector such that $0 < w_k < 1$ and $w_i = 1$ for all $0 \leq i < k$. With one optimization procedure, the weighted SSVQE is capable of obtaining the specified low-lying spectrum exactly. However, extra quantum computing resources are needed to evaluate all k expectation values within each iteration step. In the following subsections, we further describe each step for the VQE and SSVQE algorithms.

III.3. Mapping the Hamiltonian to Qubits

Here, we will discuss two suitable encoding schemes to map a hadronic Hamiltonian to qubits. Using second quantization, a generic Hamiltonian \hat{H} is represented in terms of the creation operators (\hat{a}^\dagger) and annihilation operators (\hat{a}):

$$\hat{H} = \hat{H}_1 + \hat{H}_2 + \dots = \sum_{ij} h_{ij} \hat{a}_i^\dagger \hat{a}_j + \frac{1}{4} \sum_{ijkl} h_{ijkl} \hat{a}_i^\dagger \hat{a}_j^\dagger \hat{a}_k \hat{a}_l + \dots, \quad (10)$$

where \hat{H}_1 represents the single excitation interactions, \hat{H}_2 represents the double excitation interactions and so forth. In single-particle fermion states, h_{ijkl} has a sign change under the interchange of either the first two or the last two indexes. In this work, we are working with relative coordinate representation of the meson system where the quantum properties of identical particles does not play a role. Instead, the creation operators can be viewed as symbolizing the creation of a specified mode of relative motion. For our meson system in the quark/anti-quark space, we restrict ourselves to the first term in Eq. (10) and its coefficient h_{ij} corresponds to the matrix elements in the basis representation of the BLFQ Hamiltonian. All modes accessible in the system are created by a corresponding BLFQ creation operator acting on the vacuum.

To solve the Hamiltonian problem on quantum computers in practice, we need to encode the physical states as well as any unitary operators onto the qubits. Various mapping schemes are proposed, such as the Jordan-Wigner (JW) representation [32], Bravyi-Kitaev representation [33], a compact representation [9, 17], and so forth. Here, we focus on the so-called direct encoding as described by the JW representation [32] and the compact encoding according to the Hilbert-Schmidt decomposition [34].

In the JW representation, we map directly from the fermionic operators to the many-state Pauli spin matrices. Specifically, we write the creation and annihilation operators as

$$\hat{a}_j^\dagger = \bigotimes_{i=1}^{j-1} Z_i \otimes \frac{X_j - iY_j}{2}, \quad (11)$$

$$\hat{a}_j = \bigotimes_{i=1}^{j-1} Z_i \otimes \frac{X_j + iY_j}{2}, \quad (12)$$

where X_i, Y_i, Z_i are the Pauli-X, Y, Z matrices acting on the corresponding i -th qubit. With this construction on many-qubit states, the canonical commutation relations for fermions, $\{\hat{a}_i, \hat{a}_j\} = 0$ and $\{\hat{a}_i, \hat{a}_j^\dagger\} = \delta_{ij}$, are satisfied [35]. The substitution of Eq. (11) and Eq. (12) into Eq. (10) gives rise to the desired qubitized Hamiltonian operator H_q acting on the many-qubit state. In the JW encoding, we need N qubits to encode an N -by- N Hamiltonian matrix properly, where N is always a power of two, $N = 2^n$.

In the compact representation, using the orthogonal basis formed by the Pauli strings under trace, we can decompose an N -by- N (or 2^n -by- 2^n) Hamiltonian matrix

H into its qubitized form by

$$H_q = \frac{1}{N} \sum_{\alpha=1}^{N^2} \text{Tr}(P_\alpha H) \cdot P_\alpha, \quad (13)$$

where $P_\alpha = \otimes_{k=1}^n \sigma_k$ is an n -qubit Pauli string and $\sigma_k \in \{I_k, X_k, Y_k, Z_k\}$ is a Pauli matrix acting on the k -th qubit. Since $\text{Tr}(P_\alpha P_\beta) = 2^n \delta_{j,k} = N \delta_{j,k}$ for any two P_α, P_β , and there exists $4^n = N^2$ distinct P_α , the set of all the Pauli strings form an orthogonal basis under trace for any N -by- N matrix. In this encoding, we only need $n = \log_2(N)$ qubits to encode an N -by- N matrix properly.

With either encoding scheme, the original Hamiltonian is now expressed as a sum of Pauli strings acting on the many-qubit state,

$$\hat{H} = \sum_{ij} h_{ij} \hat{a}_i^\dagger \hat{a}_j \rightarrow H_q = \sum_{\alpha} c_{\alpha} P_{\alpha}, \quad (14)$$

where P_i is a Pauli string whose length depends on the encoding and c_{α} is its respective coefficient.

III.4. Unitary Ansatzes

We now need to select a suitable ansatz $\hat{U}(\vec{\theta})$ to evolve the initial state to some final states on the quantum circuit, where $\vec{\theta}$ contains all the parameterizations of the ansatz. For JW encoding, the Unitary Coupled Cluster (UCC) [36, 37] ansatz, based on traditional coupled cluster methods, has emerged as one of the popular ansatzes. In general, the variational UCC ansatz is defined as

$$\hat{U}(\vec{\theta}) = e^{\hat{T}(\vec{\theta}) - \hat{T}^\dagger(\vec{\theta})}, \quad \hat{T}(\vec{\theta}) = \sum_{i=1}^n \hat{T}_i(\vec{\theta}) = \hat{T}_1(\vec{\theta}) + \hat{T}_2(\vec{\theta}) + \dots, \quad (15)$$

where the excitation operator \hat{T} can be written as a sum of single excitation \hat{T}_1 , double excitations \hat{T}_2 , and higher order excitations, each corresponding to its respective term in the second quantized form of the Hamiltonian. Specifically for our work within single excitation,

$$\hat{T}_1(\vec{\theta}) = \sum_{\substack{r \in \text{occ} \\ p \in \text{virt}}} \theta_p^r \hat{a}_p^\dagger \hat{a}_r, \quad (16)$$

where the *occ* and *virt* subspaces are defined as the occupied and unoccupied qubit orbital (or mode in our specific application) in the reference state, and θ_p^r are the expansion coefficients. The variational UCC ansatz allows one to span the allowed Hilbert space entirely starting from the given initial state. According to JW representation, we can show that each pair of Hermitian operators in \hat{T}_1 (for $i > j$) as

$$\hat{a}_i^\dagger \hat{a}_j - \hat{a}_j^\dagger \hat{a}_i = \frac{i}{2} \bigotimes_{a=j+1}^{i-1} Z_a (Y_j X_i - X_j Y_i) \quad (17)$$

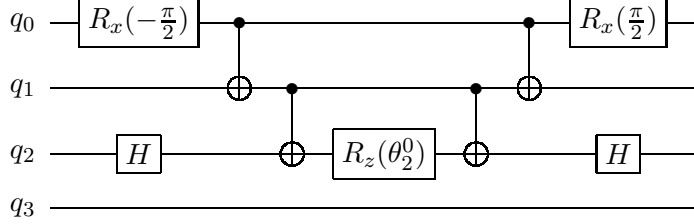


FIG. 1: Quantum circuit of one of the possible terms, $e^{\theta_2^0 \hat{a}_2^\dagger \hat{a}_0} \rightarrow e^{i\theta_2^0 X_2 Z_1 Y_0}$, in the four-qubit UCC ansatz [39] within first excitation. Here, the occupied qubit is q_0 and the virtual qubit is q_2 . The full four-qubit UCC circuit starting from a single occupied state, for example q_0 , consists of six such subcircuits in total, which makes it a very deep circuit. Note the extra factor of two in the expression is absorbed into the parameter.

and the variational ansatz can be conveniently represented as a sum of Pauli strings P_α with real coefficients c_α ,

$$\hat{U}(\vec{\theta}) = e^{i \sum_\alpha c_\alpha P_\alpha}. \quad (18)$$

The UCC unitary ansatz can be approximated via trotterization [37, 38],

$$\hat{U}(\vec{\theta}) \approx \hat{U}_{\text{Trot}}(\vec{t}) = \left(\prod_\alpha e^{i \frac{c_\alpha}{\rho} P_\alpha} \right)^\rho, \quad (19)$$

where ρ is the trotter number. In practice, the trotter number is usually quite small. We use $\rho = 1$ in this work. A partial quantum circuit of the $\hat{U}(\vec{\theta})$ is shown in Fig. 1. The UCC ansatz takes only a couple of parameters within single excitations but may result in a rather large circuit depth.

Another popular ansatz to consider is the so-called hardware efficient (HE) ansatz [31], where the circuit is composed of alternating single-qubit rotation layers and entanglement layers. The parameters of the HE ansatz are exactly the Euler angles specified in each rotation layer. The entanglement layer can have various many-qubit gate implementations to generate sufficient entanglement. The HE ansatz is a heuristic ansatz and allows us to design quantum circuits that best match a given quantum hardware layout. For the same reason, it may also be difficult to achieve the same accuracy using the HE ansatz as one achieves with the previous problem-inspired UCC ansatz. In this work, we focus on the hardware efficient SU(2) two-local ansatz, which is provided by the `qiskit.circuit.library.EfficientSU2` module [40]. For a two-qubit `EfficientSU2` ansatz with a single repetition layer, the circuit is shown in Fig. 2. Since the number of parameters in the HE ansatz scales linearly with both the number of qubits and the number of repeated layers, the HE ansatz usually takes significantly more parameters. To some extent, this can be regarded as a tradeoff between the number of parameters and the depth of the quantum circuit, which can be particularly advantageous for quantum hardware that is currently available.

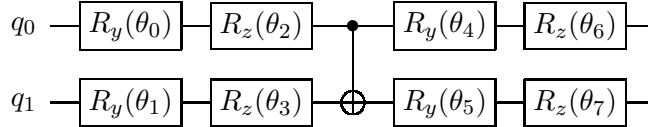


FIG. 2: Quantum circuit for the two-qubit EfficientSU2 ansatz with one single repetition layer.

III.5. Optimizers

With a parameterized unitary ansatz that takes an initial state of our choice to a final state, we are able to measure the expectation value of the Hamiltonian. Since the Hamiltonian consists of many different sub-terms, we measure each sub-term separately on the actual quantum computer. Each measurement often takes thousands of shots in order to obtain a histogram of the final quantum state. Post-measurement operations are also appended as needed, such as applying a Hadamard gate or Rotation-Y gate to change basis when measuring Pauli-Y and Pauli-X spin matrices, respectively. In the end, we obtain a single numerical value that is the best approximate of the expected eigenvalue by summing up all relevant expectations of the sub-terms in the Hamiltonian.

The measured eigenvalue is passed onto the classical computer and we use various optimizers to update the parameters for the next iteration. In this work, we used the Constrained Optimization BY Linear Approximation (COBYLA) [41–43] optimizer, the Limited-memory Broyden-Fletcher-Goldfarb-Shanno Bound (LBFGSB) [44–46] optimizer, and Sequential Least Squares Programming (SLSQP) [47] optimizer from `scipy.optimize` library. We also used the noise-resilient Simultaneous Perturbation Stochastic Approximation (SPSA) [48, 49] optimizer and the Quantum Natural SPSA (QNPSA) [50] optimizer from `qiskit.algorithms.optimizers` library. After iterated optimizations, one is expected to get the converged parameters as well as the expectation values, and, most importantly, the expected final state resulting from the given unitary ansatz.

It is crucial to run the quantum simulation multiple times as the initial starting parameters can have a large impact on the optimization outcome. In each of our results below, we have performed multiple simulations and only presented the simulation result with the lowest value of the final cost function.

IV. NUMERICAL RESULTS

IV.1. Qubitized Hamiltonian

In this work, we use the BLFQ Hamiltonian obtained from [28] in a relatively smaller basis that is more suitable to currently available quantum computing resources. We work within the $SU(2)$ isospin symmetric limit such that the anti-quark and the quark masses are identical. The values for the number of quark flavors N_f and the strong coupling coefficient are directly taken from the previous work. We limit the basis size to $(N_{\max}, L_{\max}) = (1, 1)$ and $(N_{\max}, L_{\max}) = (4, 1)$, which corresponds

to a Hamiltonian matrix dimension of 4 and 16 respectively. The quark mass m_q and the confining strength κ are obtained by fitting the experimental mass of $\rho(770)$ meson from the Particle Data Group (PDG) [51] at $N_{\max} = L_{\max} = 1$. The model parameters are summarized in Table I and they differ slightly from values in Ref. [28].

TABLE I: Model parameters of the Hamiltonian. Both Hamiltonians $H_{\text{eff}}^{(1,1)}$ and $H_{\text{eff}}^{(4,1)}$ use the same quark mass m_q and the confining strength κ at their respective basis truncations.

	N_f	$\alpha_s(0)$	κ (MeV)	m_q (MeV)	N_{\max}	L_{\max}	Matrix dimension
$H_{\text{eff}}^{(1,1)}$	3	0.89	560 ± 10	300 ± 10	1	1	4 by 4
$H_{\text{eff}}^{(4,1)}$					4	1	16 by 16

According to the basis representation of Eq. (6) and Eq. (7), the BLFQ Hamiltonian matrix for $N_{\max} = 1$ and $L_{\max} = 1$ is obtained as follows

$$H_{\text{eff}}^{(1,1)} = \begin{pmatrix} 568487 & 0 & 25428 & 0 \\ 0 & 1700976 & 0 & -15767 \\ 25428 & 0 & 568487 & 0 \\ 0 & -15767 & 0 & 1700976 \end{pmatrix}, \quad (20)$$

where each matrix element is rounded to the nearest integer and expressed in units of MeV^2 . Directly solving the Hamiltonian by matrix diagonalization on classical computers produces four eigenvalues, whose square roots correspond to the four states in the mass spectrum:

$$737 \text{ MeV}, \quad 771 \text{ MeV}, \quad 1298 \text{ MeV}, \quad 1310 \text{ MeV}, \quad (21)$$

where the second mass is fitted exactly with the experimental $\rho(770)$ meson mass.

To map the basis states of the Hamiltonian to qubits, we identify the available basis states for $N_{\max} = 1$ and $L_{\max} = 1$ as follows in Table. II. Together with Eq. (11), Eq. (12) and Eq. (13), we obtain the directly-encoded Hamiltonian operator $H_{\text{direct}}^{(1,1)}$ on 4 qubits and the compactly-encoded Hamiltonian operator $H_{\text{compact}}^{(1,1)}$ on 2 qubits respectively for the same Hamiltonian matrix $H_{\text{eff}}^{(1,1)}$,

$$\begin{aligned} H_{\text{direct}}^{(1,1)} &= 2269462 \text{ IIII} - 284243 (\text{ZIII} + \text{IIZI}) \\ &\quad - 850488 (\text{IZII} + \text{IIIZ}) + 12714 (\text{XZXI} + \text{YZYI}) \\ &\quad - 7883 (\text{IXZX} + \text{IYZY}), \end{aligned} \quad (22)$$

$$H_{\text{compact}}^{(1,1)} = 1134731 \text{ II} - 566245 \text{ IZ} + 4831 \text{ XI} + 20598 \text{ XZ}, \quad (23)$$

where each qubit operator is written as a sum of Pauli strings with the leading Pauli matrix acting on the qubit with the highest index and so on.

TABLE II: Basis state identification used in mapping from physical basis states of $(N_{\max}, L_{\max}) = (1, 1)$ to qubits. Many-qubit states are written as $|q_3q_2q_1q_0\rangle$ for direct encoding and $|q_1q_0\rangle$ for compact encoding.

	n	m	l	s	\bar{s}	Direct encoding	Compact encoding
①	0	0	0	1/2	-1/2	$ 0001\rangle$	$ 00\rangle$
②	0	0	0	-1/2	1/2	$ 0010\rangle$	$ 01\rangle$
③	0	0	1	1/2	-1/2	$ 0100\rangle$	$ 10\rangle$
④	0	0	1	-1/2	1/2	$ 1000\rangle$	$ 11\rangle$

For the Hamiltonian of $N_{\max} = 4$ and $L_{\max} = 1$, we will only focus on the compactly-encoded operator $H_{\text{compact}}^{(4,1)}$ due to the intense computational resources needed for direct encoding. The Hamiltonian operator $H_{\text{compact}}^{(4,1)}$ is included in Appendix B, and its corresponding basis identification is included in Table. VII.

IV.2. Spectroscopy

1. Results of VQE

With the Hamiltonian mapped onto the qubits, we first show the results of using the VQE algorithm to compute the ground state energy for the Hamiltonian at $N_{\max} = L_{\max} = 1$ in Fig. 3. The left panel of the figure shows the results using the directly-encoded 4-qubit operator $H_{\text{direct}}^{(1,1)}$ from Eq. (22), and the right panel shows the results using compactly-encoded 2-qubit operator $H_{\text{compact}}^{(4,1)}$ from Eq. (23). Both sets of results are in good agreement with each other and with the exact solution obtained by diagonalizing the original Hamiltonian matrix from Eq. (20). For the direct encoding, we use the 4-qubit UCC ansatz with one single trotterization and set $|0001\rangle$ as the initial state (or set q_0 as the occupied qubits), where part of the circuit is shown in Fig. 1. For the compact encoding, we use the 2-qubit `EfficientSU2` ansatz with one single repetition layer (as shown in Fig. 2) and set $|00\rangle$ as the initial state. A summary of the details of each quantum circuit is presented in Table. III. In comparison, the UCC ansatz with single excitation typically has fewer parameters but more quantum gates and a larger circuit depth.

Within each set of VQE applications, we used both the statevector (SV) simulator from `qiskit.providers.aer.StatevectorSimulator` and the qasm simulator from `qiskit.providers.aer.QasmSimulator` to simulate the quantum apparatus and calculate the ground state energy. The SV simulator is an ideal quantum circuit statevector simulator, while the qasm simulator is a noisy quantum circuit simulator. On the one hand, the SV simulator does not take into account the number of shots and returns the final quantum state vector at the end of the simulation. It is useful for debugging and theoretical testing. In Fig. 3, the LBFGBS and COBYLA optimizers

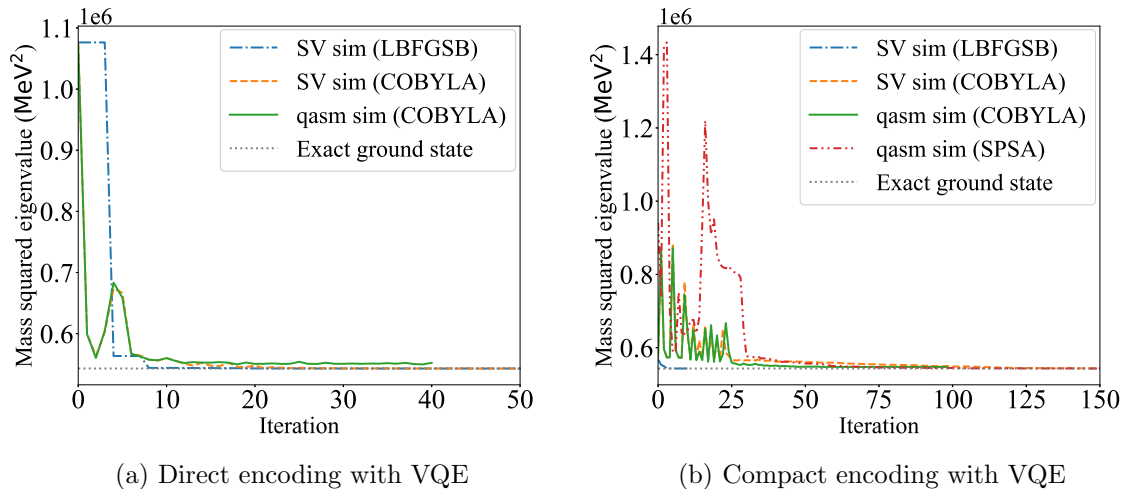


FIG. 3: The ground state energy calculated with the VQE approach using direct encoding (left panel) and compact encoding (right panel) at $N_{\max} = L_{\max} = 1$. The statevector (SV) simulator represents the ideal outcome with no shot noise, while the qasm simulator mimics the real quantum device outcome with sampling noise. Each measurement in the qasm simulator uses 8192 shots and has an average uncertainty of less than 1% that is negligible on the scale of Fig. 3. The exact ground state energy of 543058.61 MeV^2 is provided for comparison. Termination of each curve indicates the convergence of the expectation value by the respective optimizer specified in the parenthesis in the label for each result.

TABLE III: Summary of quantum circuits used in direct encoding (UCC ansatz) and compact encoding (**EfficientSU2** ansatz) after transpilation to the basis-gate set $\{ U1, U2, U3, CX \}$ with the highest optimization available in qiskit 0.18.0.

Ansatz	Qubits	Circuit depth	# parameters	# total gates	# CX-gates
UCC	4	36	3	49	20
EfficientSU2	2	5	8	9	1

are used for the SV simulator in both direct encoding and compact encoding, and they quickly converge to the expected ground state energy. On the other hand, the qasm simulator is the main Qiskit Aer backend that emulates the execution of the quantum circuit on a real device and returns measurement counts at the end of the simulation. It can be further configured to mimic an IBMQ backend by using a noise model.

In Fig. 3, we use both COBYLA and SPSA optimizers for the qasm simulators. Due to sampling noise from a measurement of 8192 shots, the results of the qasm simulator are much noisier and take longer to converge. The LBFGBS optimizer is also considered but fails to reach the expected ground state energy, as the LBFGBS

optimizer depends on derivatives of the expectation values and does not perform well with the sampling noise. The complete summary of our VQE simulation results for each optimizer and simulator backend is presented in Table. IV. For ideal simulation with the SV simulator, all results are in good agreement with the exact solution. When sampling simulation with the qasm simulator, the SPSA optimizer provides slightly better results in comparison with the COBYLA optimizer. We also used the QNPSA optimizer but its results are much noisier and slower to converge in comparison with the results from the SPSA optimizer. We found these deficiencies of the QNPSA optimizers for both the VQE and SSVQE simulations.

TABLE IV: Summary of VQE results using the statevector and qasm simulators. For qasm simulator results, sampling error is also provided from a measurement of 8192 shots. All mass values in this work are truncated to the nearest integer. Note that algorithmic iterations can have different meanings to different optimizers. The difference between the quantum simulated results and the exact energies are provided as percentages in the parenthesis.

Simulator	Encoding	Optimizer	Ground state energy (MeV ²)	Iterations
SV	Direct	LBFGSB	543059 (0%)	60
	Direct	COBYLA	543059 (0%)	90
	Compact	LBFGSB	543059 (0%)	11
	Compact	COBYLA	543059 (0%)	344
qasm	Direct	COBYLA	552344 ± 996 (1.53%)	41
	Direct	SPSA	545767 ± 152 (0.47%)	1051
	Compact	COBYLA	547405 ± 211 (0.76%)	99
	Compact	SPSA	543065 ± 6 (0%)	1551
Exact solution	-	-	543059	-

2. Results of SSVQE

By using compact encoding and the HE `EfficientSU2` ansatz, we present the results of our SSVQE approach to obtain the spectroscopy using compactly-encoded Hamiltonian operators $H_{\text{compact}}^{(1,1)}$ and $H_{\text{compact}}^{(4,1)}$ respectively. In the case of $N_{\text{max}} = L_{\text{max}} = 1$, the 4-by-4 Hamiltonian matrix is mapped onto two qubits. We prepare the four orthogonal reference states $|00\rangle, |01\rangle, |10\rangle, |11\rangle$, and then evolve them via `EfficientSU2` ansatz with two repetition layers (12 parameters in total). For the cost function, we choose the weight vector $\vec{\omega} = (1.0, 0.5, 0.25, 0.125)$ such that

$$\mathcal{C}_{\vec{\omega}} = 1.0 \cdot E_{|00\rangle} + 0.5 \cdot E_{|01\rangle} + 0.25 \cdot E_{|10\rangle} + 0.125 \cdot E_{|11\rangle}, \quad (24)$$

where $E_{|\text{state}\rangle} = \langle \text{state} | \hat{U}(\vec{\theta}) | H_{\text{compact}} | \hat{U}(\vec{\theta}) | \text{state} \rangle$ is the evolved expectation value for each orthogonal state.

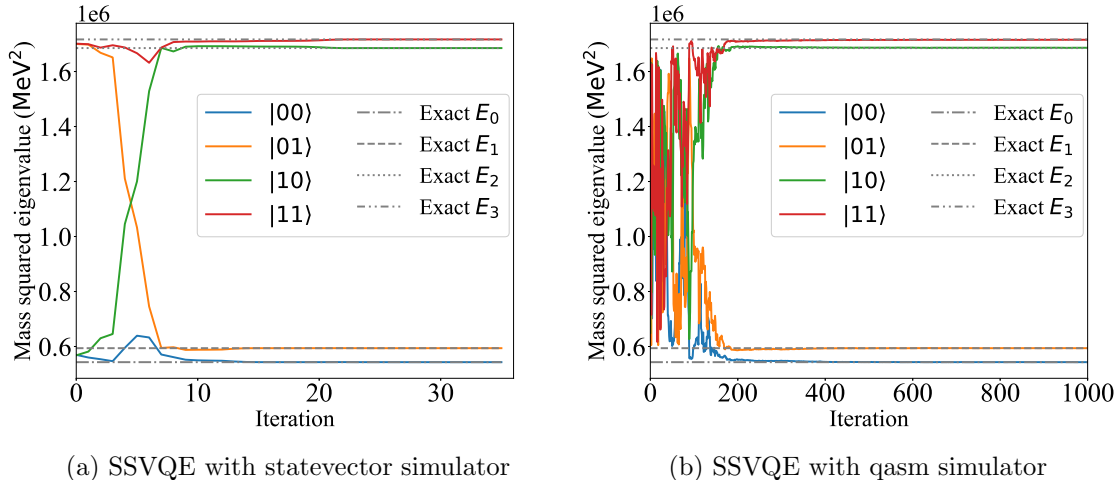


FIG. 4: The spectroscopy calculated with SSVQE approach using the statevector (SV) simulator (left panel) and the qasm simulator (right panel) at $N_{\text{max}} = L_{\text{max}} = 1$. The SV simulator uses the LBFGSB optimizer and represents the ideal outcome with no shot noise. The qasm simulator uses the SPSA optimizer and represents the real quantum device outcome with sampling noise from 8192 measurement shots. The solid curves represent the evolution of the expectation values for the four orthogonal reference states $|00\rangle, |01\rangle, |10\rangle, |11\rangle$ throughout the optimization. The grey dot-dashed, dashed, dotted, and dot-dot-dashed curves represent the exact energies E_0, E_1, E_2 and E_3 from solving the Hamiltonian directly on a classical computer.

In Fig. 4, we present the SSVQE results using the statevector (SV) and qasm simulators for $N_{\text{max}} = 1, L_{\text{max}} = 1$. The left panel shows the ideal SSVQE results using the SV simulator with the LBFGSB optimizer; the right panel shows the noisy SSVQE simulation results using the qasm simulator with the SPSA optimizer. Given any arbitrary initial parameters in the ansatz, we find both results converge to the expected exact energy states for the respective reference state in the order of their specified weight factor:

$$|00\rangle \rightarrow E_0, \quad |01\rangle \rightarrow E_1, \quad |10\rangle \rightarrow E_2, \quad |11\rangle \rightarrow E_3, \quad (25)$$

which is a significant advantage of the SSVQE approach. For the qasm simulator, the SPSA optimizer is found to be most consistent in dealing with sampling noise. The detailed numerical results for each state are summarized in Table. V.

In the case of $N_{\text{max}} = 4, L_{\text{max}} = 1$, we also use compact encoding and map the 16-by-16 Hamiltonian onto four qubits. We prepare the four orthogonal reference states $|0000\rangle, |0001\rangle, |0010\rangle, |0011\rangle$, and then evolve them via **EfficientSU2** ansatz with six repetition layers (56 parameters in total). We choose the same cost function

TABLE V: Summary of SSVQE results using the statevector and qasm simulators. For qasm simulator results, sampling error is also provided from a measurement of 8192 shots. The “SV sim” column presents the final converged SV simulator results, and the “qasm sim” column presents the final converged qasm simulator results. The difference between the quantum simulated results and the exact energies are provided as percentages in the parenthesis.

N_{\max}	L_{\max}	State	Exact energy (MeV ²)	SV sim (MeV ²)	qasm sim (MeV ²)
1	1	00⟩	543059	543059 (0%)	543059 ± 0 (0%)
		01⟩	593915	593915 (0%)	593915 ± 0 (0%)
		10⟩	1686541	1685210 (0.08%)	1686541 ± 70 (0%)
		11⟩	1715577	1716743 (0.07%)	1715577 ± 66 (0%)
4	1	0000⟩	180012	180802 (0.44%)	189263 ± 6511 (1.08%)
		0001⟩	402071	405796 (0.93%)	419139 ± 6324 (1.73%)
		0010⟩	493293	499376 (1.23%)	532381 ± 7008 (5.21%)
		0011⟩	742530	774189 (4.26%)	745422 ± 6503 (2.88%)

as shown previously in Eq. (24) except that we expect

$$|0000\rangle \rightarrow E_0, \quad |0001\rangle \rightarrow E_1, \quad |0010\rangle \rightarrow E_2, \quad |0011\rangle \rightarrow E_3. \quad (26)$$

The SSVQE results for these four states are presented in Fig. 5 with both the statevector and qasm simulator. The detailed numerical results for each state are included in Table. V. Despite having a much more complicated ansatz, we are able to obtain the results within around 5% of the exact low-lying spectroscopy with the SSVQE approach given enough iterations. We can also observe that as N_{\max} increases, the Hamiltonian is able to generate an increasing mass gap between the ground state and the first excited state, which is a desirable feature for simulating the $\pi - \rho$ mass splitting.

IV.3. Decay constants

Decay constants are experimentally important quantities and are defined as the local vacuum-to-hadron matrix element of the quark current operators. By taking the “+” current component and the $m_j = 0$ state of the meson [21], the pseudoscalar decay constants (f_P) and vector meson decay constants (f_V) in the BLFQ basis function

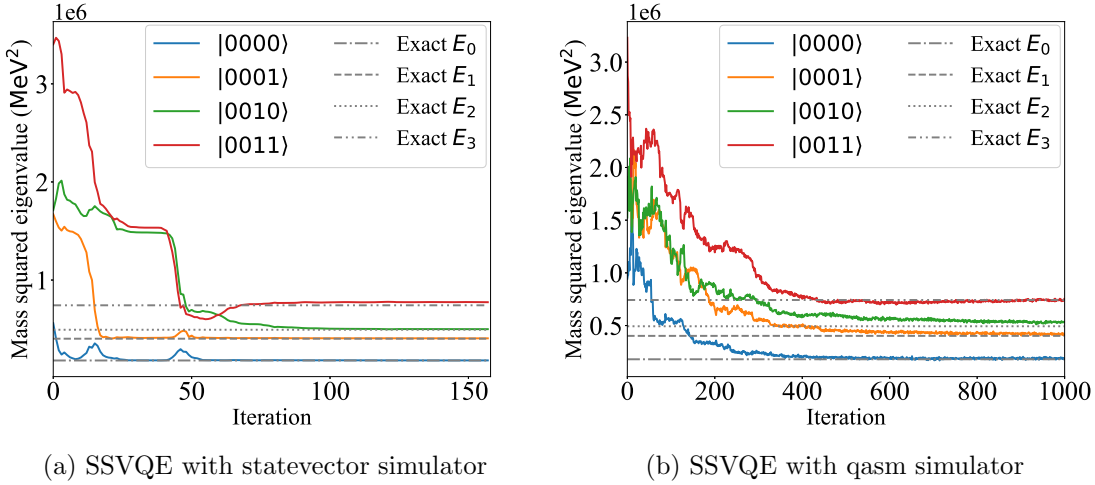


FIG. 5: The low-lying spectroscopy calculated with the SSVQE approach using the statevector (SV) simulator (left panel) and qasm simulator (right panel) at $N_{\max} = 4$, $L_{\max} = 1$. The SV simulator uses the LFGSB optimizer and represents the ideal outcome with no shot noise. The qasm simulator uses the SPSA optimizer and represents the real quantum device outcome with sampling noise from 8192 measurement shots. The solid curves represent the evolution of the expectation values for the four orthogonal reference states $|0000\rangle$, $|0001\rangle$, $|0010\rangle$, $|0011\rangle$ throughout the optimization. The grey dot-dashed, dashed, dotted, and dot-dot-dashed curves represent the four lowest-lying states E_0 , E_1 , E_2 and E_3 of the light meson bound-state system from solving the Hamiltonian directly on a classical computer.

are written as

$$f_{P,V} = 2\sqrt{2N_c} \int_0^1 \frac{dx}{2\sqrt{x(1-x)}} \int \frac{d^2\mathbf{k}_\perp}{(2\pi)^3} \psi_{\uparrow\downarrow\uparrow\downarrow}^{(m_j=0)}(x, \mathbf{k}_\perp) \quad (27)$$

$$\equiv \frac{\kappa\sqrt{N_c}}{\pi} \sum_{nl} (-1)^n C_l(m_q, \kappa) \left(\tilde{\psi}_{\uparrow\downarrow}^{(m_j=0)}(n, 0, l) \mp \tilde{\psi}_{\downarrow\uparrow}^{(m_j=0)}(n, 0, l) \right), \quad (28)$$

where C_l is the resulting coefficient that depends on m_q^2/κ [52] and $\tilde{\psi}_{s\bar{s}}^{(m_j=0)}$ is the basis coefficient of the LFWF defined in Eq. (5). In this case, the decay constants are now linear with the LFWF, $f_{P,V} \propto \langle \nu_{P,V} | \psi(\vec{\theta}) \rangle$, for some vector $\nu_{P,V}$ which depends on the specific basis identification between LFWF basis and qubits. To measure the decay constant directly on quantum computers [9], we first construct the Pauli operators from $|\nu\rangle\langle\nu|$, such that

$$|\langle \nu_{P,V} | \psi(\vec{\theta}) \rangle| = \sqrt{\langle \psi(\vec{\theta}) | (|\nu_{P,V}\rangle\langle\nu_{P,V}|) | \psi(\vec{\theta}) \rangle}, \quad (29)$$

and then map $|\nu_{P,V}\rangle\langle\nu_{P,V}|$ onto qubits by compact encoding to obtain the decay constant operators $|\nu_{P,V}\rangle\langle\nu_{P,V}|_q$. We are now able to calculate the decay constants

on the quantum computer as the expectation value of the $|\nu_{P,V}\rangle\langle\nu_{P,V}|_q$ operator on the specified final state.

For $N_{\max} = L_{\max} = 1$, according to Table. II, $\nu_P^{(1,1)} = (1, -1, 0, 0)$ and $\nu_V^{(1,1)} = (1, 1, 0, 0)$, each corresponding to the singlet and triplet LFWFs in Eq. (28) respectively. By mapping the vectors to qubits, we have

$$|\nu_P^{(1,1)}\rangle\langle\nu_P^{(1,1)}|_q = 0.5 (II - IX + ZI - ZX), \quad (30)$$

$$|\nu_V^{(1,1)}\rangle\langle\nu_V^{(1,1)}|_q = 0.5 (II + IX + ZI + ZX), \quad (31)$$

where P stands for the pseudoscalar meson and V stands for the vector meson. The decay constant operators for $N_{\max} = 4, L_{\max} = 1$ are more involved and are included in Appendix C.

In the SSVQE spectroscopy, the lowest two states are identified as the pseudoscalar meson π and the vector meson ρ . With their respective evolved final states, their decay constants are measured as the expectation value of $|\nu\rangle\langle\nu|$ using Eq. (29) and presented in Table. VI. By taking sampling error into account, we can see that the obtained decay constants from the qasm simulators are in good agreement with those from the SV simulators as well as with the exact calculation. With a limited basis size at $N_{\max} = 4, L_{\max} = 1$, our Hamiltonian provides results that are in reasonable agreement with the experimental decay constants of π (130 MeV) and ρ (216 MeV).

TABLE VI: Summary of decay constants for π and ρ by measuring final states obtained the SSVQE results using the SV and qasm simulators. The sampling error is also provided from a measurement of 8192 shots for the qasm simulators. The experimental decay constants for π and ρ are 130 MeV and 216 MeV respectively [51]. The difference between the quantum simulated results and the exact results are omitted as all results are in agreement with each other by taking into account of the uncertainty.

N_{\max}	L_{\max}	Decay constants	Exact result (MeV)	SV sim (MeV)	qasm sim (MeV)
1	1	f_π	178.18	178.18	178.17 ± 1.97
		f_ρ	178.18	178.18	178.17 ± 1.97
4	1	f_π	193.71	193.32	194.28 ± 15.49
		f_ρ	231.00	232.93	225.72 ± 13.44

IV.4. Parton distribution function

The parton distribution function (PDF) is another important experimentally-accessible quantity that is often discussed in the QCD scale evolution. It describes the probability of finding a particle with longitudinal momentum fraction x at some

factorization scale μ related to the experimental conditions. In the BLFQ basis representation [20, 53], the PDF for finding a quark in the meson system, is expressed as

$$q(x; \mu) = \frac{1}{x(1-x)} \sum_{s\bar{s}} \int \frac{d^2\mathbf{k}_\perp}{2(2\pi)^3} |\psi_{s\bar{s}}^{(m_j=0)}(x, \mathbf{k}_\perp)|^2 \quad (32)$$

$$\equiv \frac{1}{4\pi} \sum_{s\bar{s}} \sum_{nm} \sum_{\bar{l}} \tilde{\psi}_{s\bar{s}}^{*(m_j=0)}(n, m, \bar{l}) \tilde{\psi}_{s\bar{s}}^{(m_j=0)}(n, m, l) \chi_l(x) \chi_{\bar{l}}(x), \quad (33)$$

where $\tilde{\psi}_{s\bar{s}}^{(m_j=0)}$ is the basis coefficient of the LFWF defined in Eq. (5) and the PDF satisfies the normalization $\int_0^1 q(x) dx = 1$. The truncation to a Fock space with a single quark and anti-quark implies the model Hamiltonian is appropriate to a factorization scale typically much lower than the scale accessed in high-energy experiments that measure the PDF.

To compute the PDF on quantum computers, we decompose the sum and evaluate each term respectively by using projection operator $\hat{U}_p(s, \bar{s}, n, m, l)$ that map the quantum state into the corresponding basis,

$$q(x) = \sum_{s\bar{s}} \sum_{nm} \sum_{\bar{l}} \langle \psi(\vec{\theta}) | \hat{O}_{\text{pdf}}(x) | \psi(\vec{\theta}) \rangle, \quad (34)$$

where $\hat{O}_{\text{pdf}}(x) = \hat{U}_p(s, \bar{s}, n, m, \bar{l})^\dagger \hat{U}_p(s, \bar{s}, n, m, l) \chi_l(x) \chi_{\bar{l}}(x) / 4\pi$ is the unitary operator to evaluate each subterm contribution of the PDF at a given longitudinal momentum fraction x . The qubitization of the PDF operator is straightforward and we present examples of the operator at $x = 0.5$ and $x = 0.25$ in Appendix D for comparison.

By taking the lowest two states obtained from SSVQE calculations, we demonstrate the calculation of PDFs on qasm simulators for the π and ρ mesons using Eq. (34) in Fig. 6 respectively. Both sets of obtained PDFs are sampled at 19 evenly-spaced longitudinal momentum fractions and they are in reasonable agreement with those from the exact classical results. Results from SV simulators are omitted as they are almost identical to the exact calculations. In calculating the PDFs for the case of $N_{\text{max}} = 4, L_{\text{max}} = 1$, we observe slight violation of the normalization since the SSVQE results presented in Fig. 5 do not evolve to the exact final states, and therefore we have rescaled the PDFs for the case of $N_{\text{max}} = 4, L_{\text{max}} = 1$. It is also important to see that the PDFs for the pseudoscalar and the vector mesons are almost identical due to the lack of longitudinal excitation modes in both truncations. However, the strategy of computing distribution functions or observables on quantum computers is general and can be applied to other calculations as well as extended to higher basis truncations, where longitudinal excitations will differentiate these PDFs.

V. SUMMARY AND DISCUSSIONS

In this work, we used the variational quantum eigensolver (VQE) and the subspace-search variational quantum eigensolver (SSVQE) to study the hadron structures of the light meson system within the basis light-front quantization (BLFQ) approach.

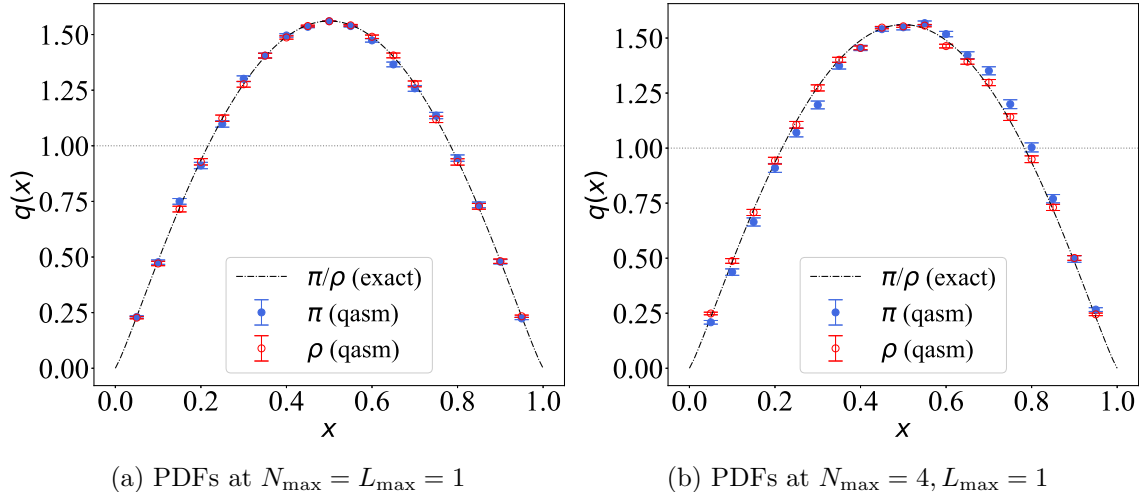


FIG. 6: The PDFs calculated with the lowest two states obtained with the SSVQE approach at $(N_{\max}, L_{\max}) = (1, 1)$ and $(N_{\max}, L_{\max}) = (4, 1)$ using the qasm simulator. The qasm simulator uses the SPSA optimizer and represents the real quantum device outcome with sampling noise from 8192 measurement shots. The dot-dashed curves represent the exact PDFs for the π and ρ mesons calculated on classical computers, which are almost identical in both numerical truncations considered in this work. The qasm simulated results of the PDFs are calculated at 19 evenly-spaced longitudinal momentum fractions and the sampling errors from a measurement of 8192 shots are also provided as their error bars respectively. The average error of the qasm PDFs are between 1% and 2%.

Our model Hamiltonian was taken from a previous work with fitted parameters obtained for two reduced basis spaces, $(N_{\max}, L_{\max}) = (1, 1)$ and $(N_{\max}, L_{\max}) = (4, 1)$. Mass spectroscopy, decay constants, and parton distribution functions (PDF) were calculated by using VQE/SSVQE approach on both the statevector simulator and the qasm simulator. We obtain results that are in reasonable agreement with the exact results when solved on classical computers.

For the Hamiltonian of $(N_{\max}, L_{\max}) = (1, 1)$, we used the UCC ansatz with direct encoding and the hardware efficient ansatz with compact encoding to obtain the lowest energy state using the VQE method. The results are consistent with the exact solution classically. For the Hamiltonian of $(N_{\max}, L_{\max}) = (4, 1)$, we used the hardware efficient ansatz with compact encoding to obtain the four lowest energy states in the spectroscopy using the SSVQE method. In addition, we also compute the decay constants for the lowest two states, which correspond to the π and ρ mesons. For all of our results, both statevector and qasm simulators are used for exact simulation and sampling simulation respectively. In general, we find COBYLA, LBFGSB and SLSQP optimizers perform well for statevector simulators; while COBYLA and SPSA perform well for qasm simulators, which is expected for the derivative-free optimizers. All of our quantum-simulated results presented in this work are in good agreement with direct classical calculations - i.e. within 5% of the exact results.

This work represents a first step to study low-lying spectroscopy within the BLFQ

formalism on quantum simulators. The VQE/SSVQE approaches prove to be useful tools for Hamiltonian formalisms. In the future, we expect to include higher basis state contributions for a more accurate description of the light meson bound-state problem. We also plan to carry out the calculations on real quantum computer backends as they become accessible. In addition, we anticipate extending our work to compute other important hadronic properties such as transition amplitudes using the SSVQE approach.

ACKNOWLEDGEMENTS

We wish to thank M. Kreshchuk, M. Li, and M. Eshaghian-Wilner for valuable discussions. This work was supported in part by the US Department of Energy (DOE), Office of Science, under Grant No. DE-FG02-87ER40371. We acknowledge the use of IBM Quantum services for this work. The views expressed are those of the authors, and do not reflect the official policy or position of IBM or the IBM Quantum team.

Appendix A: Light-front coordinates

The light-front coordinates are defined as $x^\mu = (x^+, x^-, x^1, x^2)$, where $x^+ = x^0 + x^3$ is the light-front time, $x^- = x^0 - x^3$ is the longitudinal coordinate, $\mathbf{x}^\perp = (x^1, x^2)$ are the transverse coordinates. The corresponding metric tensor and its inverse are,

$$g_{\mu\nu} = \begin{pmatrix} 0 & 1/2 & 0 & 0 \\ 1/2 & 0 & 0 & 0 \\ 0 & 0 & -1 & 0 \\ 0 & 0 & 0 & -1 \end{pmatrix}, \quad g^{\mu\nu} = \begin{pmatrix} 0 & 2 & 0 & 0 \\ 2 & 0 & 0 & 0 \\ 0 & 0 & -1 & 0 \\ 0 & 0 & 0 & -1 \end{pmatrix}. \quad (\text{A1})$$

Appendix B: Hamiltonian operator for $N_{\max} = 4$, $L_{\max} = 1$

In the case of $N_{\max} = 4$, $L_{\max} = 1$, the Hamiltonian operator in the compact representation is

$$\begin{aligned}
H_{\text{compact}}^{(4,1)} = & 1868696 \text{IIII} - 623614 \text{IIIZ} + 518799 \text{IIXI} + 44344 \text{IIXZ} \\
& - 531599 \text{IIZI} + 11950 \text{IIZZ} + 29183 \text{IYIY} - 21316 \text{IYXY} \\
& + 28874 \text{IYYI} + 22502 \text{IYYX} - 1474 \text{IYYZ} + 6301 \text{IYZY} \\
& + 1762 \text{XXII} + 7092 \text{XXIZ} - 310 \text{XXXI} - 4214 \text{XXXZ} \\
& + 653 \text{XXZI} + 3207 \text{XXZZ} + 77283 \text{XZII} - 61720 \text{XZIX} \\
& + 4548 \text{XZIZ} - 38263 \text{XZXI} + 33154 \text{XZXX} - 3510 \text{XZZX} \\
& + 844 \text{XZYY} + 19387 \text{XZZI} - 15666 \text{XZZX} + 2304 \text{XZZZ} \\
& + 29183 \text{YIIY} - 21316 \text{YIXY} - 28874 \text{YIYI} + 22502 \text{YIYX} \\
& + 1474 \text{YIYZ} + 6301 \text{YIZY} + 1762 \text{YYII} + 7092 \text{YYIZ} \\
& - 310 \text{YYXI} - 4214 \text{YYXZ} + 653 \text{YYZI} + 3207 \text{YYZZ} \\
& - 77283 \text{ZXII} - 61720 \text{ZXIX} - 4548 \text{ZXIZ} + 38263 \text{ZXXI} \\
& + 33154 \text{ZXXX} + 3510 \text{ZXXZ} + 844 \text{ZXYX} - 19387 \text{ZXZI} \\
& - 15666 \text{ZXZX} - 2304 \text{ZXZZ} + 215302 \text{ZZII} - 34396 \text{ZZIZ} \\
& + 70683 \text{ZZXI} + 19390 \text{ZZXZ} - 12936 \text{ZZZI} - 11024 \text{ZZZZ}, \tag{B1}
\end{aligned}$$

and the corresponding basis identification is included in Table. VII.

Appendix C: Decay constant operators

In the case of $N_{\max} = 4$, $L_{\max} = 1$, according to Table. VII, the vectors ν for the decay constants are defined as

$$\nu_P = (1, -1, 0, 0, 0, 0, 0, 0, -1, 1), \tag{C1}$$

$$\nu_V = (-1, -1, 0, 0, 0, 0, 0, 0, 1, 1), \tag{C2}$$

and the corresponding decay constant operators on the qubits in compact encoding are

$$\begin{aligned}
|\nu_P\rangle\langle\nu_P|_q = & 0.25 \left(\text{IIII} - \text{IIIX} + \text{IIZI} - \text{IIZX} \right. \\
& + \text{IZII} - \text{IZIX} + \text{IZZI} - \text{IZZX} \\
& - \text{XIII} + \text{XIIX} - \text{XIZI} + \text{XIZX} \\
& \left. - \text{XZII} + \text{XZIX} - \text{XZZI} + \text{XZZX} \right), \tag{C3}
\end{aligned}$$

$$\begin{aligned}
|\nu_V\rangle\langle\nu_V|_q = & 0.25 \left(\text{IIII} + \text{IIIX} + \text{IIZI} + \text{IIZX} \right. \\
& + \text{IZII} + \text{IZIX} + \text{IZZI} + \text{IZZX} \\
& - \text{XIII} - \text{XIIX} - \text{XIZI} - \text{XIZX} \\
& \left. - \text{XZII} - \text{XZIX} - \text{XZZI} - \text{XZZX} \right). \tag{C4}
\end{aligned}$$

TABLE VII: Basis state identification used in mapping from physical basis states of $(N_{\max}, L_{\max}) = (4, 1)$ to qubits. Many-qubit states are written as $|q_3q_2q_1q_0\rangle$.

	n	m	l	s	\bar{s}	Compact encoding
①	0	0	0	1/2	-1/2	0000⟩
②	0	0	0	-1/2	1/2	0001⟩
③	0	0	1	1/2	-1/2	0010⟩
④	0	0	1	-1/2	1/2	0011⟩
⑤	0	1	0	-1/2	-1/2	0100⟩
⑥	0	1	1	-1/2	-1/2	0101⟩
⑦	0	-1	0	1/2	1/2	0110⟩
⑧	0	-1	1	1/2	1/2	0111⟩
⑨	1	0	0	1/2	-1/2	1000⟩
⑩	1	0	0	-1/2	1/2	1001⟩
⑪	1	0	1	1/2	-1/2	1010⟩
⑫	1	0	1	-1/2	1/2	1011⟩
⑬	1	1	0	-1/2	-1/2	1100⟩
⑭	1	1	1	-1/2	-1/2	1101⟩
⑮	1	-1	0	1/2	1/2	1110⟩
⑯	1	-1	1	1/2	1/2	1111⟩

Appendix D: Parton distribution function operators

We present examples of the qubitized parton distribution function (PDF) operators $\hat{O}_{\text{pdf}}(x)$ at $x = 0.5$ and $x = 0.25$ (up to second decimal places) in compact encoding,

$$\hat{O}_{\text{pdf}}^{(1,1)}(0.5)_q = 1.30 II - 1.29 IX - 0.18 IZ, \quad (\text{D1})$$

$$\hat{O}_{\text{pdf}}^{(1,1)}(0.25)_q = 0.78 (II + IZ), \quad (\text{D2})$$

$$\hat{O}_{\text{pdf}}^{(4,1)}(0.5)_q = 0.39 (IIII + IIIZ - ZZII - ZZIZ), \quad (\text{D3})$$

$$\hat{O}_{\text{pdf}}^{(4,1)}(0.25)_q = 0.65 (IIII - IIIX - ZZII + ZZIX) + 0.09 (ZZIZ - IIIZ). \quad (\text{D4})$$

[1] J. Preskill, Quantum **2**, 79 (2018).

- [2] E. Farhi, J. Goldstone, and S. Gutmann, arXiv e-prints , arXiv:1411.4028 (2014), arXiv:1411.4028 [quant-ph].
- [3] A. Peruzzo, J. McClean, P. Shadbolt, M.-H. Yung, X.-Q. Zhou, P. J. Love, A. Aspuru-Guzik, and J. L. O'Brien, Nature Communications **5**, 4213 (2014), arXiv:1304.3061 [quant-ph].
- [4] D. Wecker, M. B. Hastings, and M. Troyer, Phys. Rev. A **92**, 042303 (2015).
- [5] J. R. McClean, J. Romero, R. Babbush, and A. Aspuru-Guzik, New Journal of Physics **18**, 023023 (2016).
- [6] A. G. Taube and R. J. Bartlett, International Journal of Quantum Chemistry **106**, 3393 (2006), <https://onlinelibrary.wiley.com/doi/pdf/10.1002/qua.21198>.
- [7] E. F. Dumitrescu, A. J. McCaskey, G. Hagen, G. R. Jansen, T. D. Morris, T. Papenbrock, R. C. Pooser, D. J. Dean, and P. Lougovski, Phys. Rev. Lett. **120**, 210501 (2018), arXiv:1801.03897 [quant-ph].
- [8] M. Kreshchuk, S. Jia, W. M. Kirby, G. Goldstein, J. P. Vary, and P. J. Love, Entropy **23** (2021), 10.3390/e23050597.
- [9] M. Kreshchuk, S. Jia, W. M. Kirby, G. Goldstein, J. P. Vary, and P. J. Love, Phys. Rev. A **103**, 062601 (2021), arXiv:2011.13443 [quant-ph].
- [10] J. R. McClean, M. E. Kimchi-Schwartz, J. Carter, and W. A. de Jong, Phys. Rev. A **95**, 042308 (2017).
- [11] J. I. Colless, V. V. Ramasesh, D. Dahlen, M. S. Blok, M. E. Kimchi-Schwartz, J. R. McClean, J. Carter, W. A. de Jong, and I. Siddiqi, Phys. Rev. X **8**, 011021 (2018).
- [12] O. Higgott, D. Wang, and S. Brierley, Quantum **3**, 156 (2019).
- [13] T. Jones, S. Endo, S. McArdle, X. Yuan, and S. C. Benjamin, Phys. Rev. A **99**, 062304 (2019).
- [14] J. S. Kottmann, A. Anand, and A. Aspuru-Guzik, arXiv e-prints , arXiv:2011.05938 (2020), arXiv:2011.05938 [quant-ph].
- [15] K. M. Nakanishi, K. Mitarai, and K. Fujii, Physical Review Research **1**, 033062 (2019), arXiv:1810.09434 [quant-ph].
- [16] K. Bharti, A. Cervera-Lierta, T. H. Kyaw, T. Haug, S. Alperin-Lea, A. Anand, M. Degroote, H. Heimonen, J. S. Kottmann, T. Menke, W.-K. Mok, S. Sim, L.-C. Kwek, and A. Aspuru-Guzik, "Noisy intermediate-scale quantum (nisq) algorithms," (2021), arXiv:2101.08448 [quant-ph].
- [17] M. Kreshchuk, W. M. Kirby, G. Goldstein, H. Beauchemin, and P. J. Love, arXiv e-prints , arXiv:2002.04016 (2020), arXiv:2002.04016 [quant-ph].
- [18] J. P. Vary, H. Honkanen, J. Li, P. Maris, S. J. Brodsky, A. Harindranath, G. F. de Teramond, P. Sternberg, E. G. Ng, and C. Yang, Phys. Rev. **C81**, 035205 (2010), arXiv:0905.1411 [nucl-th].
- [19] P. Wiecki, Y. Li, X. Zhao, P. Maris, and J. P. Vary, Phys. Rev. **D91**, 105009 (2015), arXiv:1404.6234 [nucl-th].
- [20] Y. Li, P. Maris, X. Zhao, and J. P. Vary, Phys. Lett. **B758**, 118 (2016), arXiv:1509.07212 [hep-ph].
- [21] Y. Li, P. Maris, and J. P. Vary, Phys. Rev. **D96**, 016022 (2017), arXiv:1704.06968 [hep-ph].
- [22] M. Li, Y. Li, P. Maris, and J. P. Vary, Phys. Rev. **D98**, 034024 (2018), arXiv:1803.11519 [hep-ph].

- [23] S. Tang, Y. Li, P. Maris, and J. P. Vary, *Phys. Rev.* **D98**, 114038 (2018), arXiv:1810.05971 [nucl-th].
- [24] S. Tang, Y. Li, P. Maris, and J. P. Vary, *Eur. Phys. J. C* **80**, 522 (2020), arXiv:1912.02088 [nucl-th].
- [25] G. Chen, Y. Li, K. Tuchin, and J. P. Vary, *Phys. Rev.* **C100**, 025208 (2019), arXiv:1811.01782 [nucl-th].
- [26] L. Adhikari, Y. Li, M. Li, and J. P. Vary, *Phys. Rev.* **C99**, 035208 (2019), arXiv:1809.06475 [hep-ph].
- [27] S. Jia and J. P. Vary, *Phys. Rev. C* **99**, 035206 (2019), arXiv:1811.08512 [nucl-th].
- [28] W. Qian, S. Jia, Y. Li, and J. P. Vary, *Phys. Rev. C* **102**, 055207 (2020).
- [29] G. F. de Teramond and S. J. Brodsky, *Phys. Rev. Lett.* **102**, 081601 (2009), arXiv:0809.4899 [hep-ph].
- [30] S. J. Brodsky, G. F. de Teramond, H. G. Dosch, and J. Erlich, *Phys. Rept.* **584**, 1 (2015), arXiv:1407.8131 [hep-ph].
- [31] A. Kandala, A. Mezzacapo, K. Temme, M. Takita, M. Brink, J. Chow, and J. Gambetta, *Nature* **549**, 242 (2017).
- [32] P. Jordan and E. P. Wigner, *Z. Phys.* **47**, 631 (1928).
- [33] S. B. Bravyi and A. Y. Kitaev, *Annals of Physics* **298**, 210 (2002), arXiv:quant-ph/0003137 [quant-ph].
- [34] M. A. Nielsen and I. L. Chuang, *Quantum Computation and Quantum Information* (Cambridge University Press, 2010).
- [35] M. A. Nielsen, “The fermionic canonical commutation relations and the jordan-wigner transform,” (2005).
- [36] M. R. Hoffmann and J. Simons, *The Journal of Chemical Physics* **88**, 993 (1988), <https://doi.org/10.1063/1.454125>.
- [37] J. Romero, R. Babbush, J. R. McClean, C. Hempel, P. J. Love, and A. Aspuru-Guzik, *Quantum Science and Technology* **4**, 014008 (2018).
- [38] M. Suzuki, *Commun. Math. Phys.* **51**, 183 (1976).
- [39] P. K. Barkoutsos, J. F. Gonthier, I. Sokolov, N. Moll, G. Salis, A. Fuhrer, M. Ganzhorn, D. J. Egger, M. Troyer, A. Mezzacapo, S. Filipp, and I. Tavernelli, *Phys. Rev. A* **98**, 022322 (2018), arXiv:1805.04340 [quant-ph].
- [40] M. S. ANIS, H. Abraham, AduOffei, R. Agarwal, G. Agliardi, M. Aharoni, I. Y. Akhalwaya, G. Aleksandrowicz, T. Alexander, M. Amy, S. Anagolum, E. Arbel, A. Asfaw, A. Athalye, A. Avkhadiev, *et al.*, “Qiskit: An open-source framework for quantum computing,” (2021).
- [41] M. J. D. Powell, “A direct search optimization method that models the objective and constraint functions by linear interpolation,” in *Advances in Optimization and Numerical Analysis*, edited by S. Gomez and J.-P. Hennart (Springer Netherlands, Dordrecht, 1994) pp. 51–67.
- [42] M. J. D. Powell, *Acta Numerica* **7**, 287–336 (1998).
- [43] M. Powell, *Mathematics TODAY* **43** (2007).
- [44] R. H. Byrd, P. Lu, and J. Nocedal, *SIAM Journal on Scientific Computing* (1994).
- [45] C. Zhu, R. Byrd, P. Lu, and J. Nocedal, *ACM Transactions on Mathematical Software* **23**, 550 (1997).
- [46] J. L. Morales and J. Nocedal, *ACM Trans. Math. Softw.* **38** (2011), 10.1145/2049662.2049669.

- [47] D. Kraft, *A software package for sequential quadratic programming*, Deutsche Forschungs- und Versuchsanstalt für Luft- und Raumfahrt Köln: Forschungsbericht (Wiss. Berichtswesen d. DFVLR, 1988).
- [48] J. Spall, *IEEE Transactions on Automatic Control* **37**, 332 (1992).
- [49] J. Spall, in *Proceedings of the 36th IEEE Conference on Decision and Control*, Vol. 2 (1997) pp. 1417–1424 vol.2.
- [50] J. Gacon, C. Zoufal, G. Carleo, and S. Woerner, arXiv e-prints , arXiv:2103.09232 (2021), arXiv:2103.09232 [quant-ph].
- [51] P. Zyla *et al.* (Particle Data Group), *PTEP* **2020**, 083C01 (2020).
- [52] W. Qian, *Relativistic bound states within Basis Light-Front Quantization*, Ph.D. thesis, Iowa State University (2020).
- [53] Y. Li, *Ab initio approach to quantum field theories on the light front*, Ph.D. thesis, Iowa State University (2015).